

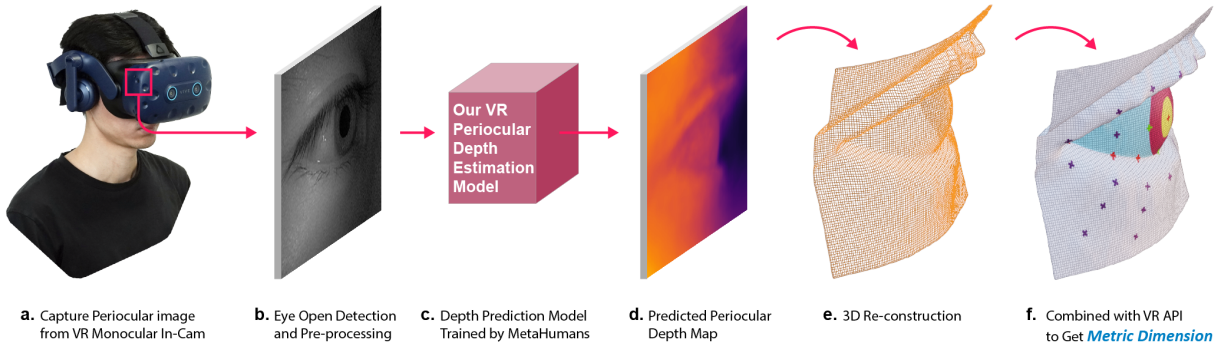
# DeepMetricEye: Metric Depth Estimation in Periocular VR Imagery

Yitong Sun\*  
Royal College of Art

Zijian Zhou†  
University of Edinburgh

Cyriel Diels‡  
Royal College of Art

Ali Asadipour§  
Royal College of Art



## ABSTRACT

Despite the enhanced realism and immersion provided by VR headsets, users frequently encounter adverse effects such as digital eye strain (DES), dry eye, and potential long-term visual impairment due to excessive eye stimulation from VR displays and pressure from the mask. Recent VR headsets are increasingly equipped with eye-oriented monocular cameras to segment ocular feature maps. Yet, to compute the incident light stimulus and observe periocular condition alterations, it is imperative to transform these relative measurements into metric dimensions. To bridge this gap, we propose a lightweight framework derived from the U-Net 3+ deep learning backbone that we re-optimised, to estimate measurable periocular depth maps. Compatible with any VR headset equipped with an eye-oriented monocular camera, our method reconstructs three-dimensional periocular regions, providing a metric basis for related light stimulus calculation protocols and medical guidelines. Navigating the complexities of data collection, we introduce a Dynamic Periocular Data Generation (DPDG) environment based on UE MetaHuman, which synthesises thousands of training images from a small quantity of human facial scan data. Evaluated on a sample of 36 participants, our method exhibited notable efficacy in the periocular global precision evaluation experiment, and the pupil diameter measurement.

**Index Terms:** Computing methodologies—Artificial intelligence—Computer vision—Computer vision tasks; Applied computing—Life and medical sciences—Consumer health

## 1 INTRODUCTION

Virtual Reality (VR) technology has advanced rapidly, offering immersive experiences across applications including gaming, medical, education, and training simulations [1, 2]. The recent re-imagining of the ‘Digital Universe’ concept has illuminated a compelling vision of globally interconnected interactions [3, 4]. Despite the continual enhancement in content quality, the use of VR headsets persists in causing physiological discomfort to users, leading to substantially

reduced usage duration [5, 6]. A significant proportion of unsatisfactory experiences by VR users can be attributed to digital eye strain (DES), dry eye, and visual impairment resulting from excessive artificial light stimulation from VR displays, as well as periocular swelling, increased intraocular pressure, and muscle displacement induced by the pressure exerted by the headset’s face mask [7]. However, these visual health issues have not yet received attention proportionate to the development of VR technology.

Recent VR headsets, increasingly equipped with eye-oriented monocular cameras, are designed to segment periocular feature maps, annotate the edge of the pupil, and detect gaze direction to enhance content interaction [8, 9]. While these methods offer a preliminary insight into eye activity during VR usage, they are insufficient for establishing connections with medical standards, for instance, the light stimulus calculation protocols and periocular condition medical guidelines, needed for meticulous visual health assessments and advanced user interaction studies [10, 11]. The fundamental issue lies in the inability of current methods to convert the segmented 2D relative feature annotations (such as pupil edge segmentation) into spatial metrics (pupil diameter), essential for strict standards. Proposed solutions, for instance, incorporating stereo cameras and depth cameras for metric size acquisition, present substantial challenges in terms of cost, computational power, battery life, and hardware design of VR headsets.

To convert 2D periocular feature annotations into 3D metric dimensions, we propose a framework that only utilises an eye-oriented monocular camera, present in various VR headsets, to estimate the measurable periocular depth map. This framework, built on a U-Net 3+ deep learning backbone, re-optimised by us, aims to accurately estimate depth maps while maintaining the lightweight processing demands suitable for VR deployment [12]. To alleviate the difficulty in collecting facial data for training, we introduce a Dynamic Periocular Data Generation (DPDG) environment that leverages a small quantity of real facial scan data to generate thousands of synthetic periocular images and corresponding ground truth depth maps using Unreal Engine (UE) MetaHuman [13]. Fig. 1 provides the snapshot of this paper.

The main contributions of this study are as follows:

1. We introduce a lightweight depth estimation framework for VR headsets to reconstruct periocular depth maps. The aim is to provide features’ metric size for light stimulus standards calculation and periocular condition monitoring.

\*e-mail: yitong.sun@network.rca.ac.uk

†e-mail: z.zhou-89@sms.ed.ac.uk

‡e-mail: cyriel.diels@rca.ac.uk

§e-mail: ali.asadipour@rca.ac.uk

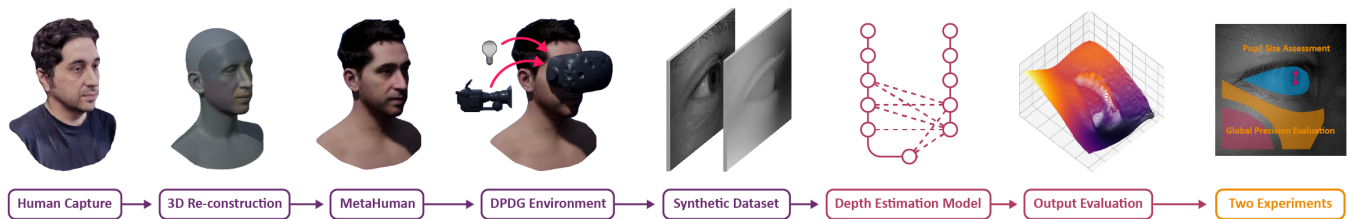


Figure 1: A Snapshot of the paper.

2. Addressing the challenge of facial data collection, our DPDG environment, based on UE MetaHuman, generates thousands of periocular training images and depth maps from limited facial scans.
3. We evaluate our method’s accuracy and usability with two tasks: 1) evaluating global precision of periocular area, and 2) assessing pupil diameter.
4. We have open-sourced the DPDG environment, the code and dataset for the depth estimation model, and all metadata from the experiments.

## 2 RELATED WORK

### 2.1 Depth Estimation

Depth estimation is vital in computer vision, with broad applications such as autonomous driving and VR indoor space reconstruction [14]. Traditional methods rely on stereo vision, estimating depth from disparity across multiple camera views, albeit with high computational demands and need for accurate camera calibration [15]. Active depth estimation technologies, using lasers or structured light to generate depth point clouds, offer high accuracy but suffer from slow scanning speeds, high computational needs, and large structure volumes [16, 17].

The emergence of image-based depth estimation has sparked research interest [18]. Eigen et al. pioneered the deep learning approach for monocular image-based depth estimation using an encoder-decoder network to transform RGB images into depth maps [19]. Subsequent advances include the integration of features like transformers, attention, and residual connections, enhancing model performance but increasing computational demands [20–23].

U-Net, initially designed for medical image segmentation, found application in depth estimation due to its simplicity and practicality [24–26]. U-Net++, proposed by Zongwei et al., introduced dense skip connections but fell short of fully exploiting multiscale information [27]. To address this, U-Net 3+ was proposed by Huimin et al., using dense skip connections across all encoder and decoder layers, reducing parameter count while improving accuracy [12].

For lightweight, robust depth estimation suitable for VR deployment, we chose U-Net 3+ as our backbone, removing shallow dense skip connections to focus on skin and eye surfaces. Deep decoder layers were weighted differently to control detail decoding, aiming to reduce noise details such as eyebrows and eyelashes.

### 2.2 Eye and Periocular Feature Segmentation

Eye tracking has widespread applications in sectors such as advertising, healthcare, education, and gaming [28]. Within VR, gaze detection has been pivotal in identifying users’ areas of interest and enhancing content interaction [29]. Furthermore, it’s extensively utilised in research and healthcare for understanding attention, behavioural patterns, and emotional shifts [30–32]. Periocular feature segmentation has also been researched to reconstruct facial expressions, acquire iris information, and locate pupils [33–35].

Deep learning has substantially improved periocular feature segmentation accuracy and efficiency compared to traditional methods [36–38]. For instance, the EyeNet framework, with residual units and attention blocks, significantly reduced recognition rate drops caused by flickering and blur noise [39]. GazeNet provides end-to-end eye movement detection, focusing on automatic event annotation without pre-labeling [40].

Despite these advancements, most methods focus on two-dimensional image features, which can’t be translated into metrical dimensions in three-dimensional space. This limits the monitoring of eye conditions according to optical standards and medical guidelines, especially given the visual fatigue and impairment caused by VR headsets.

Our method estimates a metrically measurable depth map of the periocular region using monocular images, then combines it with eye segmentation techniques to yield arbitrary feature measurements. This approach allows for effective quantification and monitoring of stimulations on the human eye from VR screen light intrusion and changes caused by the mask pressure on the periocular region.

### 2.3 Standards and Guidelines for Periocular Conditions

Adverse effects on the human eye from VR screens, such as DES, dryness, and visual impairment due to excessive light stimulation, are becoming a focal point of research [6, 41]. The face mask’s pressure can cause elevated intraocular pressure, nerve pressure, and periorbital swelling [42]. However, despite various studies, no unified method or standard exists for evaluating VR headsets’ optical stimuli [6, 43, 44]. This gap largely stems from the need for accurate pupil area measurements to calculate photoreceptor activation according to International Commission on Illumination (CIE) and American National Standards Institute (ANSI) standards, which current VR headsets’ built-in cameras cannot perform [10, 45, 46]. Furthermore, the high contrast in VR headsets complicates stimuli assessment.

Concerning periocular pressure, preliminary studies confirm the negative impacts of varying pressure levels on ocular physiology and immersion [47]. The comprehensive Adult Medical Eye Evaluation Preferred Practice Pattern (PPP) guidelines outline measurement methods related to periocular symptoms, including muscle displacement and swelling associated with VR usage [11]. Yet, the inability of VR’s eye-oriented cameras to convert 2D images into the 3D feature information required by PPP poses a significant challenge.

Our method mitigates this by estimating the periocular area’s depth map, converting 2D images into measurable 3D facial reconstructions, and providing spatial metric information aligned with various assessment standards.

## 3 METHOD

### 3.1 Dataset Creation

**Objective and Dataset Challenge** The aim of our approach is to predict the depth map based on periocular images captured by the monocular camera within VR headsets, thereby transforming relative facial feature dimensions into metric dimensions. The supervised deep learning training requires two categories of images:

1) periocular images captured by the VR headset’s internal camera, and 2) corresponding depth maps used as ground truth for training. However, our analysis of existing periocular image databases revealed a discrepancy as none met the prerequisites for training our model [48–52]. Primarily, databases utilised for gaze, pupil and iris edge detection training do not contain associated depth maps. Moreover, their data were not obtained from the internal camera of VR headsets, which prevents effective calibration of the field of view (FOV), lens distortion, and noise distribution. Additionally, given the compact space within VR headsets, deploying a depth camera to capture depth maps that align with the position of the real camera poses a considerable challenge.

**Dataset Generation** In response to these challenges, we created a Dynamic Periocular Data Generation (DPDG) environment using UE’s MetaHuman (Fig. 2). Using this approach, we synthesised virtual humans from real scans, significant mitigating data collection challenges and enhancing dataset diversity. As a state-of-the-art virtual human system, MetaHuman facilitates precise facial feature simulations and can emulate dynamic eye movements, pupil dilation, and blinking. Initially, we procured 68 official MetaHuman avatars and subsequently scanned 52 real humans using RealityCapture to create additional MetaHumans by fitting facial meshes in UE 5 (Fig. 3 a-c) [53]. To enhance the generalisability of the dataset, these 120 MetaHumans underwent a feature-mixing process using MetaHuman Creator, culminating in the generation of 1150 unique avatars [13]. Using DPDG’s feature blending, we combined diverse makeup levels with various skin tones for realism, bolstering dataset robustness. See Appendix B (FOV2 Row10, FOV4 Row6) and C (Row6) for makeup examples.



Figure 2: The Dynamic Periocular Data Generation (DPDG) environment. **a:** MetaHumans are worn a specified model of VR headset with faux realistic lighting and camera in UE for periocular image acquisition. **b:** A captured synthetic periocular image. **c:** The corresponding depth map.

**Demographic Distribution** After creating the MetaHumans, it’s important to describe the demographic distribution among the original pool of 120, which includes characteristics such as gender, age, skin tone, and ethnicity. The diversified representation within the dataset enhances variety and, consequently, bolsters the model’s capability to generalise across different scenarios.

In terms of gender distribution, an equitable balance was sought, resulting in an even split of 50% for both male and female MetaHumans. Age representation was approached with inclusivity, accounting for individuals in various life stages including youth (15-24 years), young adults (25-44 years), middle-aged individuals (45-64 years), and the elderly (65 years and above). This approach ensures a broad age range within our data.

The variety of skin tones and ethnic backgrounds was another priority, leading to an inclusive set capturing MetaHumans with varied ethnic backgrounds and skin tones. Specifically, the dataset encompasses individuals of Asian, Caucasian, African, Hispanic

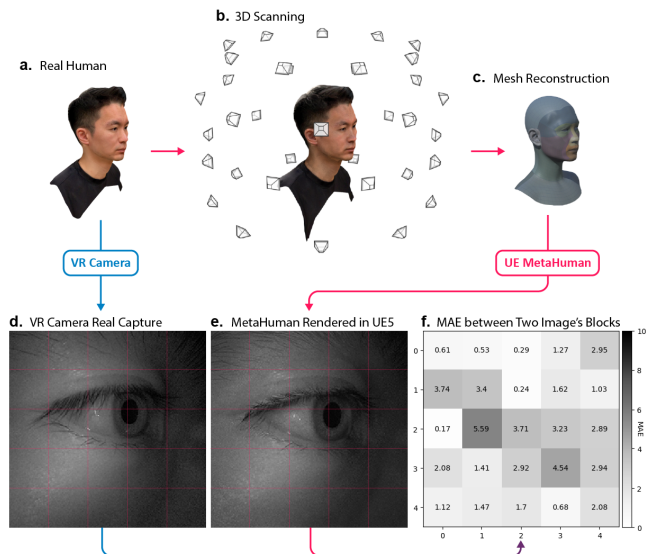


Figure 3: Process of human scan to MetaHuman, and synthetic periocular image error quantification and optimisation. **a:** Real human. **b:** 3D reconstruction of the face through RealityCapture. **c:** Converting scanned face mesh to MetaHuman. **d:** Image of the periocular taken with real VR headset. **e:** Synthetic periocular image through DPDG environment. **f:** A MAE algorithm iteratively to fine-tune the parameters of the UE cine-camera and UE PointLight to minimise the differences between real and synthetic periocular image.

backgrounds, as well as other ethnicities (mixed race). Skin tones range from fair to dark, with five categories (Fair, Light Medium, Medium, Medium Dark, Dark) considered in our MetaHuman distribution. It should be noted that due to the constraints of the VR headset capturing only in the IR spectrum, considerations for skin tone did not involve hue, but rather the grayscale intensity under the supplementary infrared light-emitting diodes (IR LEDs) illumination.

Table 1 provides a detailed breakdown of the MetaHuman distribution across the aforementioned demographic characteristics:

Attribute	Category	Count	Percentage
Gender	Male	60	50%
	Female	60	50%
Age	Youth (15-24 years)	26	21.67%
	Young Adult (25-44 years)	36	30%
	Middle-aged (45-64 years)	37	30.83%
	Elderly (65 years and above)	21	17.5%
Skin Tone	Fair	26	21.67%
	Light Medium	32	26.67%
	Medium	30	25%
	Medium Dark	17	14.17%
	Dark	15	12.5%
Ethnicity	Asian	24	20%
	Caucasian	36	30%
	African	24	20%
	Hispanic	24	20%
	Other	12	10%

Table 1: Distribution characteristics of original 120 MetaHumans

Utilising UE 5.2, we constructed the DPDG environment. Initially, we secured computer-aided design (CAD) models, camera datasets, and parameters of supplementary IR LED from official sources for various VR headsets, including HTC VIVE Pro Eye, HTC Vive Focus 3, Pico 4 Pro, and Varjo XR-3, to precisely align the spatial position and optical parameters of their internal cam-

eras. Fig. 4 shows the different distribution of camera positions and corresponding viewpoints in DPDG. Importing CAD models into UE, we placed UE cine-cameras, with parameters adjusted, at the VR internal camera’s location. IR LEDs were restored through UE PointLight and were eventually made into Actor blueprints [54]. A PostProcessMaterial was applied to the cine-cameras to convert RGB image to depth map image [55]. To streamline the capture process and boost user-friendliness, we composed an automated collection program based on the blueprint using the UE Editor Utility Widget [56]. The program sets the exporting image resolution, selects the VR headset model for collection, sequentially positions the 1150 avatars in the scene, and allows the simulated internal VR camera to individually capture the RGB image and corresponding depth map of each eye. Consequently, 2300 pairs of RGB periocular images and corresponding depth maps per VR headset model were collected.

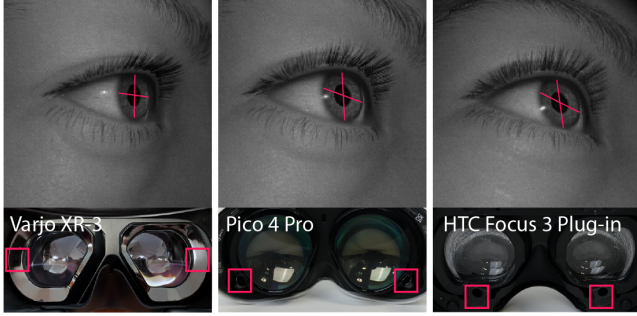


Figure 4: Distribution of monocular camera positions of three VR headsets and corresponding views in DPDG environment. The red cross indicates the perspective reference of the eyeball.

**Addressing Robustness** Recognising that the unquantified pixel colour disparities between the actual VR capture and the simulation could undermine the robustness of depth map prediction, Despite the highly accurate simulations rendered by MetaHuman, we incorporated a Mean Absolute Error (MAE) metric to quantify differences. This algorithm is used iteratively to fine-tune the parameters of the UE cine-camera and UE PointLight to minimise the differences, thereby optimising the rendering authenticity of the virtual human model.

**Error Quantification and Optimisation** Specifically, we segment each image into  $n \times n$  blocks, calculate the average pixel value for each block, and subsequently calculate the MAE between these averages. This block-based approach, rather than calculating the MAE pixel by pixel, mitigates the adverse impact of random noise and minor inconsistencies in facial feature positions on the results, focusing more on the accuracy of the overall colour transition between blocks.

Initially, we divide the actual image  $I_r$  and the simulated image  $I_s$  into  $N$  blocks. For each block  $i$ , we compute the average pixel values  $Avg_{r_i}$  for the real image and  $Avg_{s_i}$  for the simulated image as shown in the equation below:

$$Avg_i = \frac{1}{|B_i|} \sum_{x \in B_i} I_i(x) \quad \text{for } i \in r, s \quad (1)$$

Here,  $B_i$  represents the pixel count in block  $i$ , while  $I_r(x)$  and  $I_s(x)$  denote the values of pixel  $x$  in the real and simulated images in block  $i$  respectively.

The MAE for each block, denoted as  $MAE_i$ , is computed as the absolute difference between the average pixel values of the reference and the simulated image blocks, specifically  $Avg_{r_i}$  and  $Avg_{s_i}$ , respectively. Following this, we aggregate the MAEs for all the blocks to derive the total MAE, represented as  $MAE_{total}$ .

This total MAE is an average of all individual block MAEs and is calculated using the following equation:

$$MAE_{total} = \frac{1}{N} \sum_{i=1}^N |Avg_{r_i} - Avg_{s_i}| \quad (2)$$

Here, 'N' signifies the total number of blocks under consideration.

Lastly, using a gradient descent approach, we adjust the parameters of the UE cine-camera’s random noise ( $\theta_{noise}$ ) and the UE PointLight’s intensity ( $\theta_{light}$ ) to minimise the overall MAE. In each iteration, we update these parameters as a vector  $\theta = [\theta_{noise}, \theta_{light}]^T$  based on the gradient of the loss function  $L(\theta)$ , which corresponds to  $MAE_{total}$ , as expressed in the equation below:

$$\begin{bmatrix} \theta_{noise} \\ \theta_{light} \end{bmatrix} = \begin{bmatrix} \theta_{noise} \\ \theta_{light} \end{bmatrix} - \alpha \nabla L \left( \begin{bmatrix} \theta_{noise} \\ \theta_{light} \end{bmatrix} \right) \quad (3)$$

Here,  $\alpha$  is the learning rate, governing the magnitude of parameter updates at each step. We continue with this update procedure until  $L(\theta)$  reaches a minimum value that meets our threshold (0.5%), or the predetermined number of iterations is reached (is set to 100 steps).

**Error Analysis** To affirm our algorithm’s efficacy, we undertook iterative optimisation using four different VR headsets encompassed within our dataset. A representation of the terminal optimisation utilising the Varjo headset is depicted in Fig. 3 d-f. Our algorithm consistently reduced disparities between simulated and actual images, keeping the MAE below an acceptable threshold (average within 1% of the 0-255 pixel colour spectrum), affirming its effectiveness.

Given the depth map range spans from 20mm to 90mm, a 1% error corresponds to an average deviation of 0.7mm in depth estimation under optimal conditions. This degree of error is deemed acceptable for numerous measurement applications within VR. Task-specific errors will be addressed within the Experiment section.

**Limitations** It is important to recognise that the current iteration of MetaHuman is incapable of accurately reconstructing eyebrow and eyelash features, which accounts for why the MAE values of certain blocks are comparatively high. Nonetheless, the overall performance of our optimisation approach offers a robust basis for periocular depth map estimation.

## 3.2 Model Development

**Model Overview** A three-stage periocular depth estimation model is proposed in this study. Fig. 5 illustrates the framework. In the initial stage, we utilise the VR headset’s eye edge detection API to extract a series of images from the video frame flow, ensuring they align with specific eye-opening conditions. Subsequently, the selected images are iteratively input into a deep learning network, which is composed of a 5-layer symmetrical encoder-decoder, for the generation of corresponding predicted depth maps. Finally, these depth maps undergo outlier exclusion via a two-standard-deviation threshold and averaging to produce the ultimate periocular depth prediction. Further application of this model, in conjunction with the eye feature recognition API of the VR headset, allows for the calculation of metric dimensions of arbitrary features.

### 3.2.1 Data Pre-processing

**Multi-image Collection Strategy** Given the nature of wearing a VR headset, the relative position of the eye and the camera remains constant. In periocular depth estimation tasks, the process is executed as a long interval operation where accuracy of the single operation is given priority over high frame-rate processing. Therefore, we design a multi-image collection strategy for the data preparation phase. This strategy utilises built-in eye feature segmentation APIs of various VR systems to judge and collect multiple images consistent in eyelid opening degree and gaze direction. Once multiple

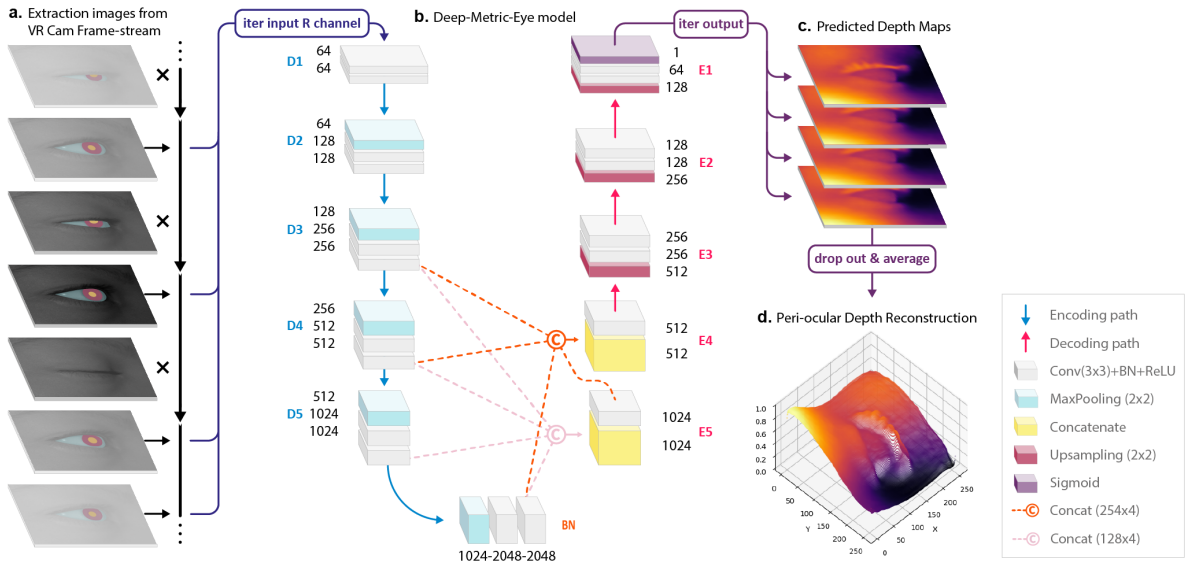


Figure 5: Flowchart of proposed depth estimation framework. **a:** Initial phase involves detection of open-eye state and gaze direction using VR headset’s API, from which a sequence of periocular images consistent with open-eye position and gaze direction is extracted from the video stream. **b:** The red channel of extracted images are iteratively input to the depth estimation model, an lightweighted and optimised U-Net 3+ variant with a 5-layer symmetrical encoder-decoder structure. The model omits shallow dense skip connections to diminish the negative impact of intricate details, such as pupils, eyelashes, and eyebrow regions, on the smooth transitions of the depth map, thereby prioritising deep semantics. The numbers indicate the depth dimensions of the tensors. **c:** The output depth maps undergo a two-standard-deviation outlier elimination and pixel averaging to produce **d**, the final periocular depth estimation.

estimated depth maps are obtained, outlier detection and processing are performed using the Median Absolute Deviation (MAD) method. MAD, a robust outlier detection method based on median absolute deviation, is less prone to extreme value impact than the standard Z-score [57]. Utilising this method effectively eliminates outliers in depth maps, and averages are taken for each pixel to improve prediction robustness.

**VR API Integration** All current VR headsets with eye-oriented cameras feature eye segmentation APIs for pupil and gaze detection. Given user privacy concerns, these APIs are proprietary. We obtained testing permissions through NDAs with HTC and PICO. For Varjo XR-3 PC VR, direct access to eye images captured by the camera is available. To ensure the complete reproducibility of the entire process, the open-source human eye segmentation framework, EllSeg, proposed by Kothari et al., was also employed as a direct-use implementation for Varjo XR-3 [58].

**Image Capture Condition** The extent of eyelid opening is crucial for tasks like facial expression recognition, fatigue detection, and depth estimation. Our method for determining eye openness is a cost-efficient computational strategy, which doesn’t necessitate a specific detection orientation and has been robustly tested within systems by Meta and HTC. The approach begins by segmenting and curve-fitting the upper and lower eyelid contours. Subsequently, it identifies the midpoint of both curves, evaluating the amplitude intervals and extremities of their movement to deduce the level of eye openness. In our study, images are captured when the gaze direction is straight ahead and the eyelids are naturally at their widest extent.

The procedure during the data preparation phase is detailed in the pseudocode provided in Appendix A, as Algorithm 2.

**Model Consideration** Transitioning from data preparation, our key challenge was designing a deep learning model suitable for the VR context, especially for standalone headsets with their computational and memory constraints. We considered architectures like DenseNet, ResNet, MonoDepth, Transformer, and Deeper Depth Prediction, all of which are renowned for depth estimation

tasks [59–63]. While these models have demonstrated significant performance in their respective domains, their inherent complexity and high parameter count make them less suitable for the constrained resources of VR applications. For instance, DenseNet’s dense connections between all layers and ResNet’s multiple stacked residual blocks, although beneficial for their specific use cases, escalate the model complexity and parameter count, posing challenges in the VR context. Increased parameters entail augmented memory and computational demands, a challenge for standalone VR headsets bereft of potent GPUs. Moreover, the inherent architectural complexity augments energy consumption, potentially hastening battery depletion and inducing latency disruptions in real-time interactions.

**Re-imagined U-Net Architecture for VR** In the evolution from PC VR to standalone VR systems, there’s a pronounced need for a lightweight yet robust deep learning model. The original U-Net architecture, commendable in its own right, faced challenges. Specifically, the classic 4-layer encoder-decoder network struggled to adequately abstract conflicting colour features, such as hair and pupils, as can be observed in the details of Figure 6. To address this, we reconfigured the U-Net blueprint. We judiciously omitted shallow skip connections, which, although beneficial for certain applications, introduced potential noise due to their emphasis on low-level features. Instead, we favoured a system that separately handles abstraction and concrete expressiveness. Further, in the deeper layers of the network, weights were assigned based on the depth of the network to each encoding layer participating in skip connections, controlling the transmission of feature details and abstraction. By augmenting the classic 4-layer structure with an additional layer, transforming it into a 5-layer symmetric structure, our model bolstered its capacity to accurately capture the nuanced depth variations inherent to the eye region. While PC-based depth estimation solutions often veer towards increased complexity, our re-imagined U-Net strikes a balance between efficiency and performance, offering a promising approach for similar challenges, especially in the context of resource-constrained VR devices.

### 3.2.2 Model Training

**Training Dataset Preparation** Model training was performed separately for each VR headset model. For each model, 2300 pairs of periorcular RGB images and corresponding ground truth depth maps, both of 256x256 resolution, were randomly apportioned into training, validation, and testing subsets, adhering to a 70%-15%-15% distribution. As the camera within the VR is equipped with a filter film that matches the wavelength of the supplementary IR LEDs to avoid screen light interference, it results in its effective light-sensitive channel being the red channel only. Therefore, during the data pre-processing stage, in order to be consistent with the VR camera and to further reduce the number of model parameters, the RGB images used for training were channel split, with only the red single channel data being extracted for training and the green and blue channels being discarded.

**Model Architecture Detail** As shown in Fig. 5 b, our model comprises a five-layer down-sampling convolutional encoder, a bottleneck layer, and a five-layer up-sampling convolutional decoder. Each layer of the five-layer encoder and the bottleneck layer employs a convolution operation with a 3x3 kernel, stride of 2, and padding of 1, followed by a ReLU activation function and batch normalisation. This sequence is repeated once within each layer. Pooling operations with a pool size and stride of 2 succeed each encoder layer, further reducing the spatial dimensions.

In the decoder part, we introduce skip connections to enable feature-sharing from the third, fourth, fifth layer of encoder and bottleneck layer with the corresponding fourth and fifth layer in the decoder. Additionally, to regulate the propagation of features during decoding, we assign varying weights to the encoder layers based on their depth. This strategic weighting ensures that our model captures and propagates the necessary level of detail during the encoding-decoding process. The specific weights applied are represented by the following function:

---

**Algorithm 1** Weights Set for Model Skip Concatenations

---

```
1: function SKIPCONCATENATE( $E3, E4, E5, BN$ )
2:    $D5 \leftarrow \text{concat}(0.1E3, 0.8E4, 1.0E5, 1.0BN)$ 
3:    $D4 \leftarrow \text{concat}(0.2E3, 0.5E4, 0.8BN, 1.0D5)$ 
4:   return  $D4, D5$ 
5: end function
```

---

The third to fifth decoder layers initially undergo a bilinear up-sampling operation with a scale of 2, succeeded by two sets of 3x3 convolutions (stride 2, padding 1), ReLU activation, and batch normalisation. Finally, we apply a 1x1 convolution, followed by a Sigmoid activation function. All convolutional layers adopt He initialisation for weights and zero initialisation for biases.

**Loss Function** The chosen loss function for our depth estimation task is the Reverse Huber Loss (BerHu). The BerHu loss function, given by Equation (4), exhibits different behaviours contingent on the magnitude of the error,  $x$ , which corresponds to the disparity between the predicted and actual depth values. The parameter  $c$  denotes a threshold, which has been set at 24% of the maximum absolute error within a mini batch after our iterative testing.

$$L_{\text{berHu}}(x) = \begin{cases} |x| & \text{if } |x| \leq c, \\ \frac{x^2+c^2}{2c} & \text{otherwise,} \end{cases} \quad (4)$$

For errors that do not exceed  $c$ , BerHu aligns with the L1 loss function, thereby functioning as an absolute error. This linear component renders the loss function resilient to outliers, mitigating their impact on the model’s learning trajectory and thereby enhancing model robustness.

In the scenario where errors exceed  $c$ , BerHu mirrors the L2 loss function, acting as a squared error. This quadratic aspect imposes more substantial penalties on larger errors. The consequential

drive to minimise these errors results in the model paying enhanced attention to such instances.

The distinct dual character of the BerHu loss function enables effective management of both minor and major prediction errors, demonstrating its suitability for depth estimation tasks.

**Regularisation** We adopt several strategies to counteract overfitting. Dropout layers, with a dropout rate of 0.5, are inserted into the fifth layer of the encoder and the bottleneck layer. Additionally, we introduce an early stopping mechanism that halts training if there is no improvement in the validation loss after 20 consecutive epochs. Training is set for a maximum of 150 epochs, starting with an initial learning rate of 1e-4.

### 3.2.3 Model Evaluation

**Evaluation and Comparative Analysis** We synthesised perspective-appropriate training datasets for various VR headsets in the DPDG environment and subjected our model to training and evaluation. To present an integrated perspective on the model’s performance, we averaged the model performance metrics across different headsets and compared them with four original structured U-Net models as the benchmark. These encompass the U-Net and U-Net 3+ models with both 4-layer and 5-layer symmetrical structures.

Multiple metrics were employed to measure depth estimation error (lower is better) and accuracy (higher is better), including Absolute Relative Difference (AbsRel), Squared Relative Difference (SqRel), Root Mean Square Error (RMSE), Logarithmic Root Mean Square Error (RMSElog), and the accuracy under thresholds of 1.25, 1.25<sup>2</sup>, and 1.25<sup>3</sup>.

The results, summarised in Table 2, clearly demonstrate that, compared to the four original U-Net models, our model consistently outperforms in terms of both depth estimation error and accuracy across all tested VR headsets, indicating substantial generalisability. Moreover, it is worth noting that our model achieves a deeper layer structure with a parameter count comparable to that of the 4-layer symmetrical U-Net 3+ model, proving to be more efficient than the other three models.

**Visualisation of Errors** For a detailed performance insight, we visualised depth estimation results from a representative image in the validation set (Fig. 6). This involved comparing our model’s estimations with the ground truth and calculating the MAE for each normalised depth value. The log-transformed MAE values, shown in a 3D plot, indicate our model’s superior accuracy, especially around the pupils and cheekbones, suggesting its utility for tasks like measuring pupil diameter. In comparison, other models struggle with regions like the pupil due to their equal focus on surface and deeper semantics.

**Analysis Summary** On the whole, our model manifests a robust performance. In comparison with the original U-Net models, our model demonstrates superior depth estimation accuracy and lower error across multiple VR headsets. Moreover, the visualisation further emphasises the advantages of our model, especially in estimating the depth of complex regions of detail and transition such as eyelashes, eyebrows, and image boundaries.

## 4 EXPERIMENT

To demonstrate our VR depth estimation model’s practical applicability, we conducted two experiments. In the **Global Precision Evaluation**, we employed the ORBBEC Femto Time of Flight (ToF) camera, chosen for its renowned near-limit accuracy in commercial devices, boasting a depth map accuracy error of only 0.2%. By comparing the depth data from participants’ periorcular regions captured by this ToF camera with our model’s estimations, this experiment aimed to evaluate our model’s global region error, assessing its potential as a feasible alternative to high-precision equipment. The **Pupil Diameter Measurement** experiment evaluated the model’s

Model	Depth Error(↓)				Depth Accuracy(↑)			Model Size(↓)
	AbsRel	SqRel	RMSE	RMSElog	$\delta < 1.25$	$\delta < 1.25^2$	$\delta < 1.25^3$	Parameters
Ours-VIVE Pro Eye	0.039	0.012	0.013	1.009	0.979	0.985	0.986	28.8M
Ours-VIVE Focus3	0.041	0.014	0.021	0.921	0.971	0.981	0.983	28.8M
Ours-Pico 4 Pro	0.037	0.012	0.018	1.109	0.969	0.986	0.982	28.8M
Ours-Varjo XR-3	0.035	0.011	0.014	1.122	0.976	0.984	0.987	28.8M
Ours Avg.	<b>0.038</b>	<b>0.012</b>	<b>0.017</b>	<b>1.040</b>	<b>0.974</b>	<b>0.984</b>	<b>0.985</b>	28.8M
U-Net 4—4-layer [24]	0.648	0.161	0.182	1.830	0.244	0.558	0.818	31.1M
U-Net 5—5-layer	0.064	0.021	0.022	1.155	0.963	0.982	0.978	53.6M
U-Net3+ 4—4-layer [26]	0.121	0.029	0.043	1.119	0.957	0.980	0.984	<b>26.9M</b>
U-Net3+ 5—5-layer	0.092	0.018	0.038	1.023	0.965	0.983	0.979	44.6M

Table 2: Comparative analysis of our model and the original structured U-Net models in terms of depth error, depth accuracy, and parameters. The depth error and parameters are preferred to be lower (represented by ↓), and depth accuracy is preferred to be higher (represented by ↑). Results are given for different VR headset datasets and the average performance is also provided. Our model consistently outperforms the U-Net models, showing superior performance across different headset datasets and maintaining a comparable model size to the 4-layer U-Net3+ model.

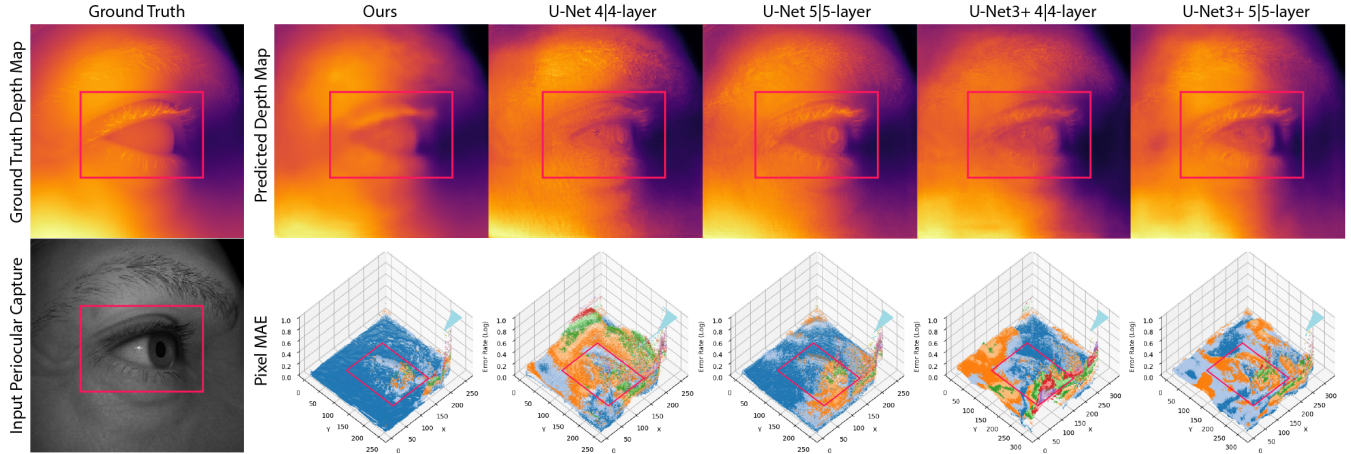


Figure 6: A three-dimensional visualisation of the MAE for the depth estimation from our model and four original structured U-Net models. The MAE values have been log-transformed to emphasise the differences. The x and y-axes represent the length and width of the image, while the z-axis represents the log-transformed MAE values. The visualisation demonstrates our model's superior depth estimation performance, particularly in intricate areas such as around the pupils and cheekbones. It highlights the benefits of our model's focus on deep semantics, and the shortcomings of models giving equal attention to both surface details and deeper semantics.

capability to measure fine details. Under constant lighting, we measured participants' pupil sizes and contrasted them with sizes from our model's depth maps. Additionally, prediction time for each depth map was recorded. Fig. 7 depicts the experimental setup.

36 participants (18-60 years, balanced by gender) with a variety of skin tones participated in our study. They were health-screened, with no vision impairments. To ensure uniformity, glasses and contact lenses were removed, and of these participants, 12 wore makeup. All participants gave informed consent after understanding the study's procedures and potential discomforts. They were informed of their right to withdraw anytime. The study was approved by the Institutional Review Board of Royal College of Art, adhering to ethical standards.

#### 4.1 Global Precision Evaluation

In the first experiment, each participant underwent two periocular data acquisitions for both the left and right eyes. Initially, participants were equipped with a PICO 4 Pro VR headset. We deployed our proposed model within the VR system using the *Pytorch Android Mobile* deployment process to estimate depth maps at a 256x256 pixel resolution. To establish a consistent baseline and counteract camera distortion, we transformed the depth map to absolute spatial coordinates using the equation:

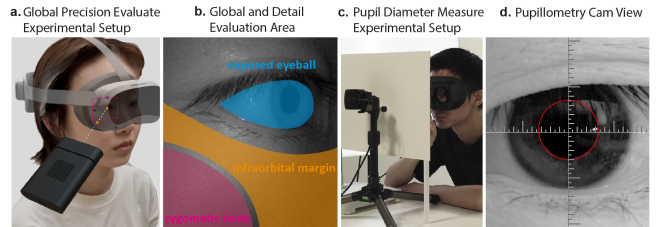


Figure 7: Experimental Setup: ORBBEC Femto ToF camera and PICO 4 Pro VR headset alignment for periocular region imaging. **b**: Illustration of the regions used for global and regional accuracy evaluation. **c**: Setup for the pupil measurement experiment. **d**: Pupillometry Camera view for pupil diameter measurement.

$$(X, Y, Z) = ((x - c_x) * s * D_p / f_x, (y - c_y) * s * D_p / f_y, s * D_p) \quad (5)$$

where  $D_p$  represents the pixel value in the depth map, while  $s$  is a conversion scaling factor used to convert pixel values into the real-world depth,  $Z$ . The coordinates  $x$  and  $y$  represent the pixel location in the image, and  $(X, Y, Z)$  are the corresponding coordinates in three-dimensional space.  $c_x$  and  $c_y$  are the positions of the optical

centre of the camera lens in the image coordinate system, typically located at the centre of the image. The terms  $f_x$  and  $f_y$  denote the focal lengths of the camera.

For the second acquisition, the Femto ToF camera was aligned to mirror the viewpoint of the PICO headset’s internal camera and was positioned 20cm away from the participant’s eye (its minimum effective focal distance), capturing periocular depth data at a 256x256 pixel resolution. The absolute coordinates were derived from the official camera API.

Upon concluding the measurements, we amassed 72 valid samples. The pixel-based Mean Absolute Error ( $MAE_p$ ) between the two depth maps was calculated to be 1.68mm, with a standard deviation ( $sd$ ) of 1.22mm across all pixels. The predominant errors, mainly observed in the eyebrow and eyelash regions, arise from the Femto camera’s limitations in effectively capturing hair. Additionally, our model’s strategic abstraction of these regions to achieve surface smoothness might also be a contributing factor to the discrepancies.

However, when focusing on regions of paramount importance for medical standards, such as the exposed eyeball, infraorbital margin, and zygomatic bone, our model showcased commendable precision. The  $MAE_p$  values for these regions were 0.63mm, 0.74mm, and 0.57mm, respectively, with  $sd$  values of 0.27mm, 0.35mm, and 0.24mm. These findings underline the potential of our approach in practical, medically-relevant scenarios. The detailed comparison results and regional discrepancies for a part of the samples are presented in Appendix D. Notably, despite the makeup variations across participants, the results remained consistent, affirming the robustness of our model, which was trained on datasets inclusive of diverse makeup levels. On average, the model required 8.11 seconds to predict a depth map.

## 4.2 Pupil Diameter Measurement

For the secondary experiment, participants were positioned in a controlled environment with consistent illumination, oriented towards a uniformly frosted cardboard sheet. Centrally, an aperture was incorporated into the cardboard to facilitate a calibrated *Baumer VCXU.2-123C* pupillometry camera, purposed for frontally gauging participants’ pupil diameters. Concurrently, participants were equipped solely with the HTC Focus 3 eye tracker. The main body of the VR headset, tethered via a USB type-c cable, was strategically placed laterally. Depth map prediction was executed via the *Pytorch Android Mobile* deployment within the VR system. The pupillometry camera and HTC eye tracker accessory operated in tandem, producing reference diameter measurements and predictive depth maps. Following this, the absolute pupil diameter was ascertained employing the VR system’s intrinsic pupil segmentation API in conjunction with equation 5. The resulting discrepancy was quantified against the reference value by computing the absolute differential between the ground truth pupil size and the size deduced from the depth map.

Notably, while corneal refraction possesses the potential to perturb pupil diameter measurements, preliminary simulations, constructed via Zemax modelling of an idealised human ocular structure, suggest that refractive aberrations owing to corneal interference are inconsequential under our experimental conditions, especially when assessing pupil diameter at oblique angles. Comprehensive specifications and resultant data from these simulations are elaborated upon in Appendix E.

Subsequent to experimental completion, a corpus of 72 valid measurement samples was curated, delineating pupil diameters spanning from 3.61mm to 4.48mm, averaging at 5.17mm. The divergence between authentic and estimated pupil diameters yielded an average ( $\mu$ ) of 0.33mm, accompanied by a standard deviation ( $sd$ ) of 0.14mm. The ensuing percentage discrepancy totaled 6.38%. The mean computational time required for depth map prediction was registered at 7.31 seconds.

## 4.3 Analysis of Results

The experimental outcomes validate the efficacy and precision of our periocular depth estimation framework in both feature measurement and micro-scale feature assessment. In the Global Precision Evaluation experiment, the model showcased high accuracy in regions critical for health standards calculation, despite diminished precision in areas covered by hair. However, in the Pupil Diameter Measurement experiment, a slight increase in error was observed. We hypothesise this discrepancy results from the limited pixel area occupied by the pupil in low-resolution images, potentially leading to imprecise pupil edge segmentation due to pixel aliasing. Addressing this limitation by enhancing acquisition resolution or employing curve fitting could refine the accuracy of micro-scale feature estimations. These findings underscore the framework’s viability for advanced eye state monitoring in VR settings, aligning with light stimulation standards and medical guidelines.

## 5 CONCLUSION

In summary, our study presents a composite framework for periocular measurable depth estimation capable of efficiently and accurately predicting spatial metric dimensions for eye region features using an eye-oriented monocular VR camera. To mitigate the challenges of facial data collection for training the model, we introduce our DPDG environment, which can generate synthetic periocular datasets for various VR headsets using MetaHuman. Through having conducted two practical experiments, the Global Precision Evaluation and the Pupil Diameter Measurement, our model has proven its robust capabilities in spatial depth estimation and detailed small-scale feature assessment. Our aim is to bridge the gap between eye and periocular state changes during VR immersion and light stimulation standards and medical guidelines, thereby facilitating deep and comprehensive monitoring, with the ultimate goal of effectively quantifying stimuli to mitigate the harm inflicted on human eyes by current VR headsets usage.

**Limitation and Future Work** Despite the successful deployment of our framework in VR, the volume of parameters remains substantial. We hypothesise that this could be due to the profusion of superfluous details in the eyelash and eyebrow areas, which may have significantly consumed network fitting efficiency and drastically increased the parameter count. To address this, a potentially effective solution might involve deleting eyelashes and eyebrows when creating ground truth depth maps within the DPDG, while preserving the details in the RGB images for model training. Another limitation is the exclusive focus on participants not wearing glasses. The presence of glasses could pose heightened challenges in depth estimation due to reflections, lens distortions, and obstructions, warranting exploration in future studies. Although the current straight-forward gaze acquisition suffices for most scenarios, we envision potential dynamic acquisition in the future by integrating 3D ocular surface reconstruction [38, 64]. Lastly, While pixel-based edge segmentation offers speed advantages, it can result in jagged edges when measuring small-scale features such as the pupil, leading to reduced accuracy. Transitioning to curve fitting might provide a more refined approach, enhancing precision.

## 6 OPEN SCIENCE

To promote further research into eye health within VR, we have made our DPDG dataset synthesis environment and the depth estimation model / code available to the public through the provided GitHub link<sup>1</sup>. For the experimental metadata containing facial information, please contact the authors and sign an NDA before accessing, to ensure the facial privacy rights of the participants.

<sup>1</sup><https://github.com/sunytong/DPDG-Env>

## REFERENCES

- [1] Ersin Dincelli and Alper Yayla. Immersive virtual reality in the age of the metaverse: A hybrid-narrative review based on the technology affordance perspective. *The journal of strategic information systems*, 31(2):101717, 2022.
- [2] Zixuan Zhang, Feng Wen, Zhongda Sun, Xinge Guo, Tianyi He, and Chengkuo Lee. Artificial intelligence-enabled sensing technologies in the 5g/internet of things era: from virtual reality/augmented reality to the digital twin. *Advanced Intelligent Systems*, 4(7):2100228, 2022.
- [3] Stylianos Mystakidis. Metaverse. *Encyclopedia*, 2(1):486–497, 2022.
- [4] Huansheng Ning, Hang Wang, Yujia Lin, Wenxi Wang, Sahraoui Dhe- lim, Fadi Farha, Jianguo Ding, and Mahmoud Daneshmand. A survey on the metaverse: The state-of-the-art, technologies, applications, and challenges. *IEEE Internet of Things Journal*, 2023.
- [5] Behrang Keshavarz and John F Golding. Motion sickness: current concepts and management. *Current opinion in neurology*, 35(1):107–112, 2022.
- [6] Teresa Hirzle, Fabian Fischbach, Julian Karlbauer, Pascal Jansen, Jan Gugenheimer, Enrico Rukzio, and Andreas Bulling. Understanding, addressing, and analysing digital eye strain in virtual reality head-mounted displays. *ACM Transactions on Computer-Human Interaction (TOCHI)*, 29(4):1–80, 2022.
- [7] Alexis D Souchet, Domitile Lourdeaux, Alain Pagani, and Lisa Reben- itsch. A narrative review of immersive virtual reality’s ergonomics and risks at the workplace: cybersickness, visual fatigue, muscular fatigue, acute stress, and mental overload. *Virtual Reality*, 27(1):19–50, 2023.
- [8] Fan Li, Ching-Hung Lee, Shanshan Feng, Amy Trappey, and Fazal Gilani. Prospective on eye-tracking-based studies in immersive virtual reality. In *2021 IEEE 24th International Conference on Computer Supported Cooperative Work in Design (CSCWD)*, pages 861–866. IEEE, 2021.
- [9] Wolfgang Fuhl, Gjergji Kasneci, and Enkelejda Kasneci. Teyed: Over 20 million real-world eye images with pupil, eyelid, and iris 2d and 3d segmentations, 2d and 3d landmarks, 3d eyeball, gaze vector, and eye movement types. In *2021 IEEE International Symposium on Mixed and Augmented Reality (ISMAR)*, pages 367–375. IEEE, 2021.
- [10] International Commission on Illumination. Cie system for metrology of optical radiation for iprgc-influenced responses to light, 2018.
- [11] Robert S Feder, Timothy W Olsen, Bruce E Prum, C Gail Summers, Randall J Olson, Ruth D Williams, and David C Musch. Comprehensive adult medical eye evaluation preferred practice pattern® guidelines. *Ophthalmology*, 123(1):P209–P236, 2016.
- [12] Huimin Huang, Lanfen Lin, Ruofeng Tong, Hongjie Hu, Qiaowei Zhang, Yutaro Iwamoto, Xianhua Han, Yen-Wei Chen, and Jian Wu. Unet 3+: A full-scale connected unet for medical image segmentation. In *ICASSP 2020-2020 IEEE International Conference on Acoustics, Speech and Signal Processing (ICASSP)*, pages 1055–1059. IEEE, 2020.
- [13] Zhixin Fang, Libai Cai, and Gang Wang. Metahuman creator the starting point of the metaverse. In *2021 International Symposium on Computer Technology and Information Science (ISCTIS)*, pages 154–157. IEEE, 2021.
- [14] Chaoqiang Zhao, Qiyu Sun, Chongzhen Zhang, Yang Tang, and Feng Qian. Monocular depth estimation based on deep learning: An overview. *Science China Technological Sciences*, 63(9):1612–1627, 2020.
- [15] Hamid Laga, Laurent Valentin Jospin, Farid Boussaid, and Mohammed Bannamoun. A survey on deep learning techniques for stereo-based depth estimation. *IEEE transactions on pattern analysis and machine intelligence*, 44(4):1738–1764, 2020.
- [16] Liang Cheng, Song Chen, Xiaoqiang Liu, Hao Xu, Yang Wu, Manchun Li, and Yanming Chen. Registration of laser scanning point clouds: A review. *Sensors*, 18(5):1641, 2018.
- [17] Song Zhang. High-speed 3d shape measurement with structured light methods: A review. *Optics and lasers in engineering*, 106:119–131, 2018.
- [18] Yue Ming, Xuyang Meng, Chunxiao Fan, and Hui Yu. Deep learning for monocular depth estimation: A review. *Neurocomputing*, 438:14–33, 2021.
- [19] David Eigen, Christian Puhrsch, and Rob Fergus. Depth map prediction from a single image using a multi-scale deep network. *Advances in neural information processing systems*, 27, 2014.
- [20] Zhaoshuo Li, Xingtong Liu, Nathan Drenkow, Andy Ding, Francis X Creighton, Russell H Taylor, and Mathias Unberath. Revisiting stereo depth estimation from a sequence-to-sequence perspective with trans- formers. In *Proceedings of the IEEE/CVF International Conference on Computer Vision*, pages 6197–6206, 2021.
- [21] Dan Xu, Wei Wang, Hao Tang, Hong Liu, Nicu Sebe, and Elisa Ricci. Structured attention guided convolutional neural fields for monocular depth estimation. In *Proceedings of the IEEE conference on computer vision and pattern recognition*, pages 3917–3925, 2018.
- [22] Xiaotian Chen, Xuejin Chen, and Zheng-Jun Zha. Structure-aware residual pyramid network for monocular depth estimation. *arXiv preprint arXiv:1907.06023*, 2019.
- [23] Yifan Jin, Lei Yu, Zhong Chen, and Shumin Fei. A mono slam method based on depth estimation by densenet-cnn. *IEEE Sensors Journal*, 22(3):2447–2455, 2021.
- [24] Olaf Ronneberger, Philipp Fischer, and Thomas Brox. U-net: Con- volutional networks for biomedical image segmentation. In *Medical Image Computing and Computer-Assisted Intervention–MICCAI 2015: 18th International Conference, Munich, Germany, October 5-9, 2015, Proceedings, Part III 18*, pages 234–241. Springer, 2015.
- [25] Nahian Siddique, Sidike Paheding, Colin P Elkin, and Vijay Devabhak- tuni. U-net and its variants for medical image segmentation: A review of theory and applications. *Ieee Access*, 9:82031–82057, 2021.
- [26] Lipu Zhou and Michael Kaess. Windowed bundle adjustment frame- work for unsupervised learning of monocular depth estimation with u-net extension and clip loss. *IEEE Robotics and Automation Letters*, 5(2):3283–3290, 2020.
- [27] Zongwei Zhou, Md Mahfuzur Rahman Siddiquee, Nima Tajbakhsh, and Jianming Liang. Unet++: A nested u-net architecture for medical image segmentation. In *Deep Learning in Medical Image Analysis and Multimodal Learning for Clinical Decision Support: 4th Inter- national Workshop, DLMIA 2018, and 8th International Workshop, ML-CDS 2018, Held in Conjunction with MICCAI 2018, Granada, Spain, September 20, 2018, Proceedings 4*, pages 3–11. Springer, 2018.
- [28] Kenneth Holmqvist, Saga Lee Örbom, Ignace TC Hooge, Diederick C Niehorster, Robert G Alexander, Richard Andersson, Jeroen S Ben- jamins, Pieter Bignaut, Anne-Marie Brouwer, Lewis L Chuang, et al. Eye tracking: empirical foundations for a minimal reporting guideline. *Behavior research methods*, 55(1):364–416, 2023.
- [29] Nandini Modi and Jaiteg Singh. A review of various state of art eye gaze estimation techniques. *Advances in Computational Intelligence and Communication Technology: Proceedings of CICT 2019*, pages 501–510, 2021.
- [30] Stephen Lisk, Ayesha Vaswani, Marian Linetzky, Yair Bar-Haim, and Jennifer YF Lau. Systematic review and meta-analysis: Eye-tracking of attention to threat in child and adolescent anxiety. *Journal of the American Academy of Child & Adolescent Psychiatry*, 59(1):88–99, 2020.
- [31] Jiannan Kang, Xiaoya Han, Jiajia Song, Zikang Niu, and Xiaoli Li. The identification of children with autism spectrum disorder by svm approach on eeg and eye-tracking data. *Computers in biology and medicine*, 120:103722, 2020.
- [32] Jia Zheng Lim, James Mountstephens, and Jason Teo. Emotion recog- nition using eye-tracking: taxonomy, review and current challenges. *Sensors*, 20(8):2384, 2020.
- [33] Wolfgang Fuhl, David Geisler, Wolfgang Rosenstiel, and Enkelejda Kasneci. The applicability of cycle gans for pupil and eyelid segmen- tation, data generation and image refinement. In *Proceedings of the IEEE/CVF International Conference on Computer Vision Workshops*, pages 0–0, 2019.
- [34] Kang Wang and Qiang Ji. Real time eye gaze tracking with 3d de- formable eye-face model. In *Proceedings of the IEEE International Conference on Computer Vision*, pages 1003–1011, 2017.
- [35] Wolfgang Fuhl, Daniel Weber, and Shahram Eivazi. Pistol: Pupil invis- ible supportive tool to extract pupil, iris, eye opening, eye movements, pupil and iris gaze vector, and 2d as well as 3d gaze. *arXiv preprint arXiv:2201.06799*, 2022.
- [36] Nasro Min-Allah, Farmanullah Jan, and Saleh Alrashed. Pupil detec-

- tion schemes in human eye: a review. *Multimedia Systems*, 27(4):753–777, 2021.
- [37] Aayush K Chaudhary, Rakshit Kothari, Manoj Acharya, Shusil Dangi, Nitinraj Nair, Reynold Bailey, Christopher Kanan, Gabriel Diaz, and Jeff B Pelz. Ritnet: Real-time semantic segmentation of the eye for gaze tracking. In *2019 IEEE/CVF International Conference on Computer Vision Workshop (ICCVW)*, pages 3698–3702. IEEE, 2019.
- [38] Yuk-Hoi Yiu, Moustafa Aboulatta, Theresa Raiser, Leoni Ophey, Virginia L Flanagan, Peter Zu Eulenburg, and Seyed-Ahmad Ahmadi. Deepvov: Open-source pupil segmentation and gaze estimation in neuroscience using deep learning. *Journal of neuroscience methods*, 324:108307, 2019.
- [39] Priya Kansal and Sabarinathan Devanathan. Eyenet: Attention based convolutional encoder-decoder network for eye region segmentation. In *2019 IEEE/CVF International Conference on Computer Vision Workshop (ICCVW)*, pages 3688–3693. IEEE, 2019.
- [40] Raimondas Zemblys, Diederick C Niehorster, and Kenneth Holmqvist. gazenet: End-to-end eye-movement event detection with deep neural networks. *Behavior research methods*, 51:840–864, 2019.
- [41] Alexis D Souchet, Stéphanie Philippe, Domitile Lourdeaux, and Laure Leroy. Measuring visual fatigue and cognitive load via eye tracking while learning with virtual reality head-mounted displays: A review. *International Journal of Human-Computer Interaction*, 38(9):801–824, 2022.
- [42] Arian Mehrfard, Javad Fotouhi, Giacomo Taylor, Tess Forster, Nassir Navab, and Bernhard Fuerst. A comparative analysis of virtual reality head-mounted display systems. *arXiv preprint arXiv:1912.02913*, 2019.
- [43] James S Wolffsohn, Gareth Lingham, Laura E Downie, Byki Huntjens, Takenori Inomata, Saleel Jivraj, Emmanuel Kobia-Acquah, Alex Muntz, Karim Mohamed-Noriega, Sotiris Plainis, et al. Tfos lifestyle: impact of the digital environment on the ocular surface. *The ocular surface*, 28:213–252, 2023.
- [44] Yan Wang, Guangtao Zhai, Sichao Chen, Xiongkuo Min, Zhongpai Gao, and Xuefei Song. Assessment of eye fatigue caused by head-mounted displays using eye-tracking. *Biomedical engineering online*, 18:1–19, 2019.
- [45] Illuminating Engineering Society ANSI/IES RP-3-13. American national standard practice on lighting for educational facilities, 2014.
- [46] International Commission on Illumination. Light and lighting — integrating lighting — non-visual effects, 2022.
- [47] Yumiao Chen, Xin Wang, and Huijia Xu. Human factors/ergonomics evaluation for virtual reality headsets: a review. *CCF Transactions on Pervasive Computing and Interaction*, 3(2):99–111, 2021.
- [48] Luiz A Zanlorensi, Rayson Laroca, Diego R Lucio, Lucas R Santos, Alceu S Britto Jr, and David Menotti. A new periocular dataset collected by mobile devices in unconstrained scenarios. *Scientific Reports*, 12(1):17989, 2022.
- [49] Luiz A Zanlorensi, Hugo Proença, and David Menotti. Unconstrained periocular recognition: Using generative deep learning frameworks for attribute normalization. In *2020 IEEE International Conference on Image Processing (ICIP)*, pages 1361–1365. IEEE, 2020.
- [50] Stephan J Garbin, Yiru Shen, Immo Schuetz, Robert Cavin, Gregory Hughes, and Sachin S Talathi. Openeds: Open eye dataset. *arXiv preprint arXiv:1905.03702*, 2019.
- [51] Joohwan Kim, Michael Stengel, Alexander Majercik, Shalini De Mello, David Dunn, Samuli Laine, Morgan McGuire, and David Luebke. Nvgaze: An anatomically-informed dataset for low-latency, near-eye gaze estimation. In *Proceedings of the 2019 CHI conference on human factors in computing systems*, pages 1–12, 2019.
- [52] Matej Vitek, Abhijit Das, Diego Rafael Lucio, Luiz Antonio Zanlorensi, David Menotti, Jalil Nourmohammadi Khiarak, Mohsen Akbari Shahpar, Meysam Asgari-Chenaghlu, Farhang Jaryani, Juan E. Tapia, Andres Valenzuela, Caiyong Wang, Yunlong Wang, Zhaofeng He, Zhenan Sun, Fadi Boutros, Naser Damer, Jonas Henry Grebe, Arjan Kuijper, Kiran Raja, Gourav Gupta, Georgios Zampoukis, Lazaros Tsochatzidis, Ioannis Pratikakis, S.V. Aruna Kumar, B.S. Harish, Umapada Pal, Peter Peer, and Vitomir Štruc. Exploring bias in sclera segmentation models: A group evaluation approach. *IEEE Transactions on Information Forensics and Security (TIFS)*, 18:190–205, 2023.
- [53] Capturing Reality. Explore the possibilities, <https://www.capturingreality.com/realitycapture>, 2023.
- [54] Unreal Engine. Point lights, <https://docs.unrealengine.com/5.2/en-us/point-lights-in-unreal-engine/>, 2023.
- [55] Unreal Engine. Post process materials, <https://docs.unrealengine.com/5.2/en-us/post-process-materials-in-unreal-engine/>, 2023.
- [56] Unreal Engine. Editor utility widgets, <https://docs.unrealengine.com/5.2/en-us/editor-utility-widgets-in-unreal-engine/>, 2023.
- [57] Alexander E Curtis, Tanya A Smith, Bulat A Ziganshin, and John A Elefteriades. The mystery of the z-score. *Aorta*, 4(04):124–130, 2016.
- [58] Rakshit S Kothari, Aayush K Chaudhary, Reynold J Bailey, Jeff B Pelz, and Gabriel J Diaz. Ellseg: An ellipse segmentation framework for robust gaze tracking. *IEEE Transactions on Visualization and Computer Graphics*, 27(5):2757–2767, 2021.
- [59] Forrest Iandola, Matt Moskewicz, Sergey Karayev, Ross Girshick, Trevor Darrell, and Kurt Keutzer. Densenet: Implementing efficient convnet descriptor pyramids. *arXiv preprint arXiv:1404.1869*, 2014.
- [60] Kaiming He, Xiangyu Zhang, Shaoqing Ren, and Jian Sun. Deep residual learning for image recognition. In *Proceedings of the IEEE conference on computer vision and pattern recognition*, pages 770–778, 2016.
- [61] Clément Godard, Oisín Mac Aodha, and Gabriel J Brostow. Unsupervised monocular depth estimation with left-right consistency. In *Proceedings of the IEEE conference on computer vision and pattern recognition*, pages 270–279, 2017.
- [62] Ashish Vaswani, Noam Shazeer, Niki Parmar, Jakob Uszkoreit, Llion Jones, Aidan N Gomez, Łukasz Kaiser, and Illia Polosukhin. Attention is all you need. *Advances in neural information processing systems*, 30, 2017.
- [63] Iro Laina, Christian Rupprecht, Vasileios Belagiannis, Federico Tombari, and Nassir Navab. Deeper depth prediction with fully convolutional residual networks. In *2016 Fourth international conference on 3D vision (3DV)*, pages 239–248. IEEE, 2016.
- [64] Kai Dierkes, Moritz Kassner, and Andreas Bulling. A novel approach to single camera, glint-free 3d eye model fitting including corneal refraction. In *Proceedings of the 2018 ACM Symposium on Eye Tracking Research & Applications*, pages 1–9, 2018.

## APPENDIX A

---

### Algorithm 2 Eye Condition Determination for Image Extraction

```

1: procedure IMGPREPROCESSING(frames, vrAPI, model, capacity)    ▷ Assume a consistent frame rate of ‘fps’ for the input frame list
2:   thresholdFrames ← first  $6 \times fps$  frames of frames           ▷ Extract initial six seconds frames for threshold determination
3:   threshold ← DETERMINETHRESHOLD(thresholdFrames, vrAPI)     ▷ Compute threshold using frames from initial six seconds
4:   eyeImages ← empty list with capacity                          ▷ Initialise a list
5:   for each frame in frames do
6:     if ISEYEOPEN(frame, vrAPI, threshold) and ISGAZE STRAIGHT(frame, vrAPI) then
7:       eyeImages.append(frame)
8:       if eyeImages.isFull() then
9:         output ← model.predict(eyeImages)                   ▷ Input images into the model for prediction
10:        eyeImages.clear()                                     ▷ Clear the list for next iteration
11:      end if
12:    end if
13:  end for
14:  return output                                             ▷ Return the final output from the model
15: end procedure
16: function DETERMINETHRESHOLD(initialFrames, vrAPI)
17:   midPointsTop ← empty list
18:   midPointsBottom ← empty list
19:   for each frame in initialFrames do
20:     if ISGAZE STRAIGHT(frame, vrAPI) then
21:       eyelidOutline ← vrAPI.getEyelidOutline(frame)         ▷ Extract the eyelid outline from the current frame
22:       curveTop ← fitCurve(eyelidOutline.topEdge)             ▷ Fit a curve to the top eyelid’s contour
23:       curveBottom ← fitCurve(eyelidOutline.bottomEdge)     ▷ Fit a curve to the bottom eyelid’s contour
24:       midTop ← getMidPoint(curveTop)                        ▷ Calculate the midpoint of the top eyelid curve
25:       midBottom ← getMidPoint(curveBottom)                 ▷ Calculate the midpoint of the bottom eyelid curve
26:       midPointsTop.append(midTop)                          ▷ Store the top eyelid midpoint for later analysis
27:       midPointsBottom.append(midBottom)                    ▷ Store the bottom eyelid midpoint for later analysis
28:     end if
29:   end for
30:   threshold ← max(midPointsTop) – min(midPointsBottom)    ▷ Determine the threshold
31:   return threshold
32: end function
33: function ISEYEOPEN(frame, api, threshold)
34:   eyelidOutline ← api.getEyelidOutline(frame)             ▷ Extract eyelid outline from frame
35:   curveTop ← api.fitCurve(eyelidOutline.topEdge)           ▷ Curve fit the top eyelid
36:   curveBottom ← api.fitCurve(eyelidOutline.bottomEdge)    ▷ Curve fit the bottom eyelid
37:   midTop ← api.getMidPoint(curveTop)                       ▷ Get midpoint of the top curve
38:   midBottom ← api.getMidPoint(curveBottom)                 ▷ Get midpoint of the bottom curve
39:   if midBottom – midTop ≥ threshold then
40:     return True                                             ▷ Return True if eye in frame is opened sufficiently
41:   else
42:     return False
43:   end if
44: end function
45: function ISGAZE STRAIGHT(frame, api)
46:   isStraight ← api.processGazeDirection(frame)
47:   return isStraight                                       ▷ Return True if the gaze in the frame is straight, False otherwise
48: end function

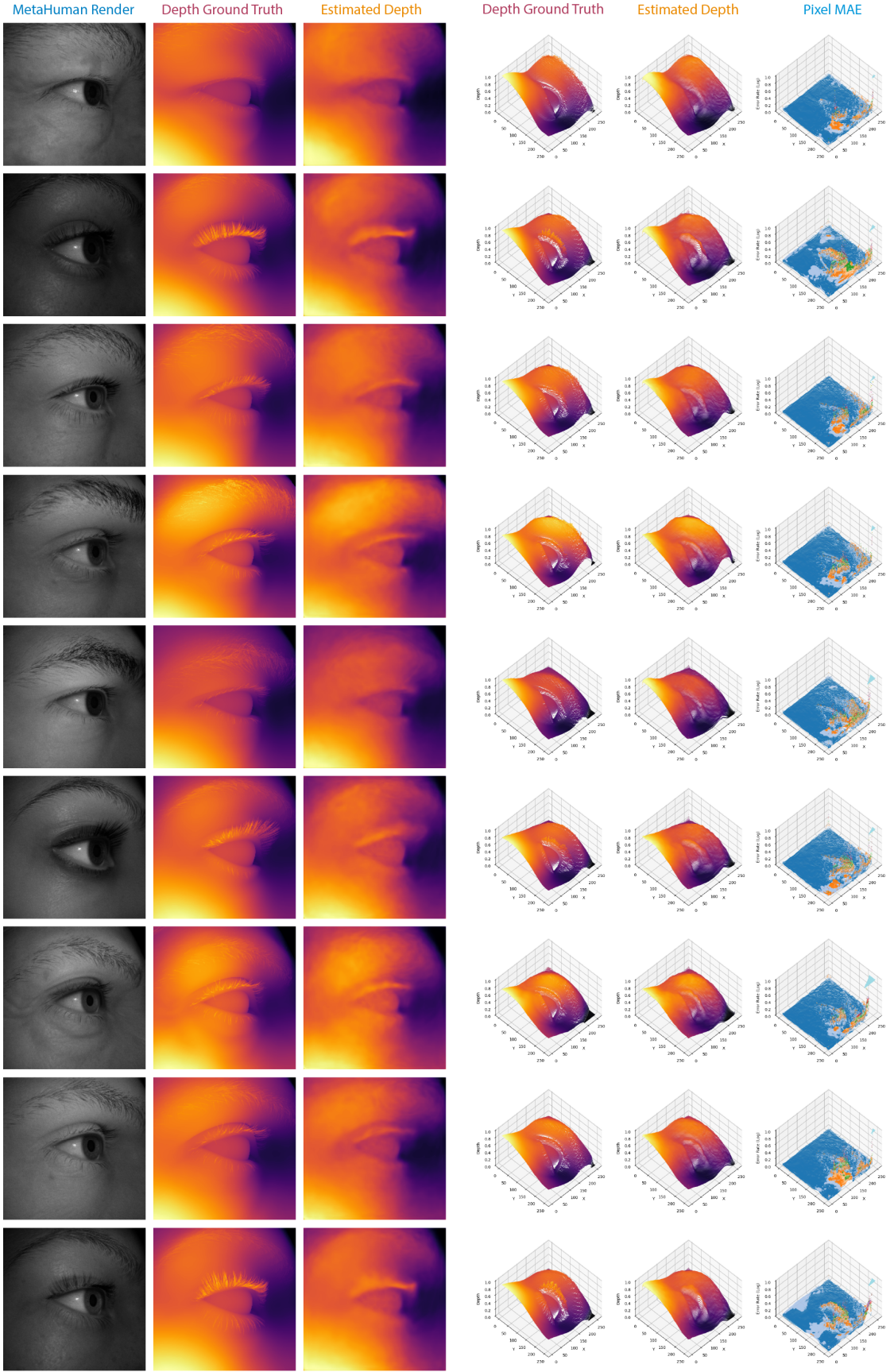
```

---

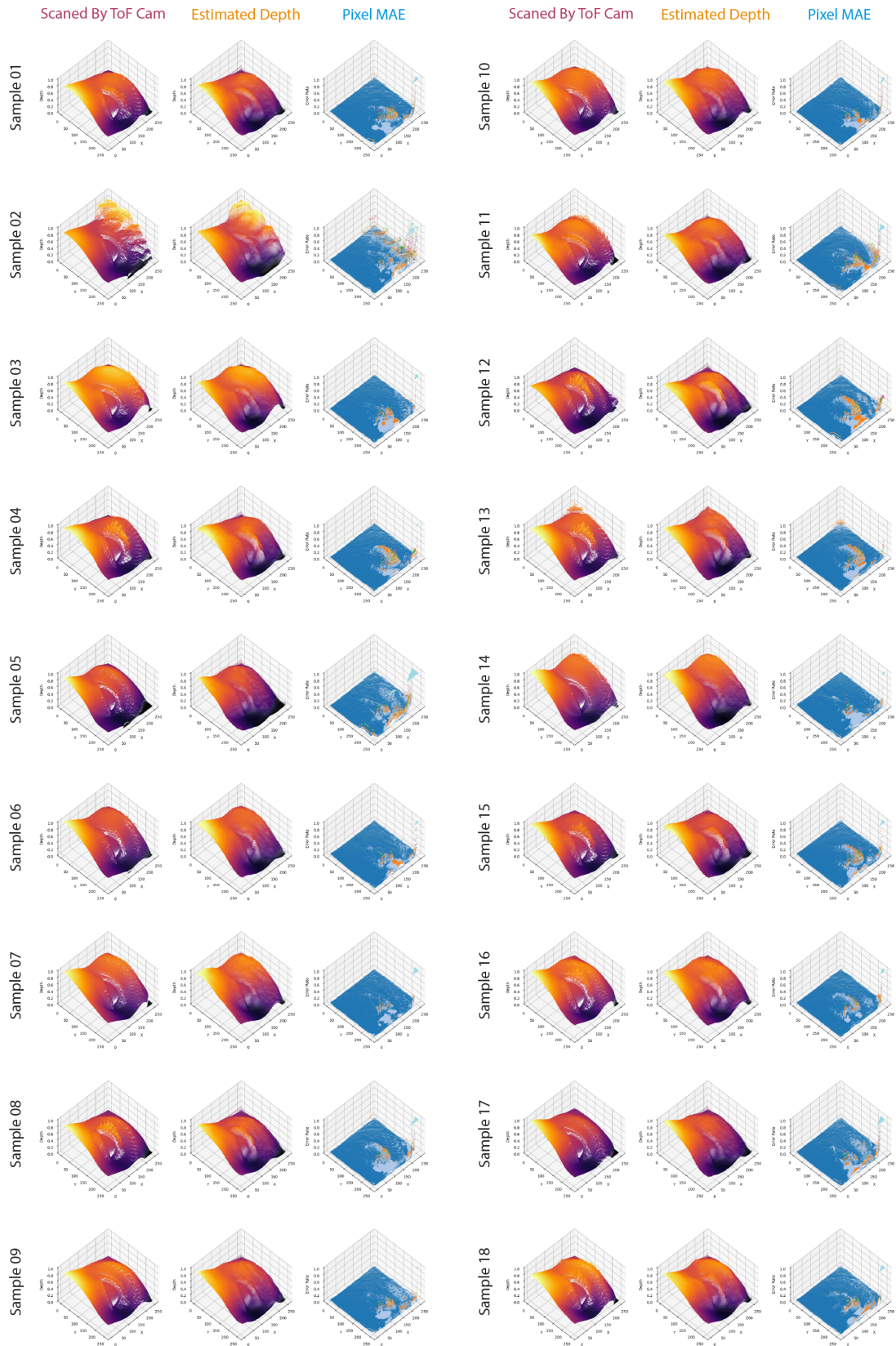
# Appendix B Example of synthetic periorcular images using DPDG environment



# Appendix C Example of Estimated Depth Map Compared to Ground Truth



# Appendix D Comparative Analysis of ToF Camera Scans and Model-Estimated Depth Maps (Sample Subset: 18 of 72)



## APPENDIX E: CORNEAL REFRACTION SIMULATIONS USING ZEMAX

In our efforts to ensure the precision of pupil diameter measurements, we conducted simulations to account for the potential effects of corneal refraction. An ideal human eye model was constructed using Zemax, with the following parameters: corneal curvature  $R = 8mm$ , anterior chamber depth  $H = 2.7mm$ , refractive index of 1.35, and pupil diameter of  $4mm$ .

The table below presents the results from the simulation, indicating the actual pupil size, observed size when viewed externally, and the error percentage from angles ranging from  $0^\circ$  to  $60^\circ$ .

Angle ( $^\circ$ )	Actual (mm)	Observed (mm)	Error (%)
0	4.00	4.00	0.01
10	4.00	4.01	0.18
20	4.00	4.01	0.31
30	4.00	4.02	0.52
40	4.00	4.03	0.75
50	4.00	4.04	0.89
60	4.00	4.04	1.02

Table 3: Simulation results illustrating the effect of angle on observed pupil size.

From the simulation, it was determined that the maximum area differential, when observing from a frontal view to a  $60^\circ$  camera rotation, was a mere 1.02%. This minute deviation justifies our assertion that refractive effects can be considered negligible for the pupil diameter measurements in our experimental setup.

## APPENDIX F: GLOSSARY OF TERMS

AI	Artificial Intelligence
AbsRel	Absolute Relative Difference
ANSI	American National Standards Institute
API	Application Programming Interface
BerHu	Reverse Huber Loss
CAD	Computer-aided Design
CNN	Convolutional Neural Network
CIE	Commission on Illumination
DES	Digital Eye Strain
DPDG	Dynamic Periocular Data Generation
FOV	Field of View
IR LED	Infrared Light-emitting Diode
RMSE	Root Mean Square Error
RMSElog	Logarithmic Root Mean Square Error
RGB	Red Green Blue
GPU	Graphics Processing Unit
MAE	Mean Absolute Error
MAD	Median Absolute Deviation
NDA	Non-Disclosure Agreement
PPP	Preferred Practice Pattern
SqRel	Squared Relative Difference
ToF	Time of Flight
UE	Unreal Engine
VR	Virtual Reality